

Supplementary Information for Characterization of a two-transmon processor with individual single-shot qubit readout

A. Dewes¹, F. R. Ong¹, V. Schmitt¹, R. Lauro¹, N. Boulant², P. Bertet¹, D. Vion¹, and D. Esteve¹

¹*Quantronics group, Service de Physique de l'État Condensé (CNRS URA 2464),*

IRAMIS, DSM, CEA-Saclay, 91191 Gif-sur-Yvette, France and

²*I2BM, Neurospin, LRMN, 91191CEA-Saclay, 91191 Gif-sur-Yvette, France*

(Dated: December 8, 2011)

I. SAMPLE PREPARATION AND EXPERIMENTAL SETUP

- **Sample fabrication:** the sample is fabricated on a silicon chip oxidized over 50 nm. A 150 nm thick niobium layer is first deposited by magnetron sputtering and then dry-etched in a SF_6 plasma to pattern the readout resonators, the current lines for frequency tuning, and their ports. Finally, the transmon qubit, the coupling capacitance and the Josephson junctions of the resonators are fabricated by double-angle evaporation of aluminum through a shadow mask patterned by e-beam lithography. The first layer of aluminum is oxidized in a $Ar - O_2$ mixture to form the oxide barrier of the junctions. The chip is glued with wax on a printed circuit board (PCB) and wire bonded to it. The PCB is then screwed in a copper box anchored to the cold plate of a dilution refrigerator.
- **Qubit microwave pulses:** The qubit drive pulses are generated by two phase-locked microwave generators whose continuous wave outputs are fed to a pair of I/Q-mixers. The two IF inputs of each of these mixers are provided by a 4-Channel 1 GS/s arbitrary waveform generator (AWG Tektronix AWG5014). Single-sideband mixing in the frequency range of 50 – 300 MHz is used to generate multi-tone drive pulses and to obtain a high ON/OFF ratio (> 50 dB) of the signal at the output of the mixers. Phase and amplitude errors of the mixers are corrected by measuring the signals at the output and applying sideband and carrier frequency dependent corrections in amplitude and offset to the IF input channels.
- **Flux Pulses:** The flux control pulses are generated by a second AWG and sent to the chip through a transmission line, equipped with 40 dB of attenuation distributed over different temperature stages and a pair of 1 GHz absorptive low-pass filters at 4 K. The input signal of each flux line is fed back to room temperature through an identical transmission line and is then measured to compensate the non-ideal frequency response of the line.
- **Readout Pulses:** The pulses for the Josephson bifurcation amplifier (JBA) readouts are generated by mixing the continuous signals of a pair of microwave generators with IF pulses provided by a 1 GS/s arbitrary function generator. Each readout pulse consists of a measurement part with a rise time of 30 ns and a hold time of 100 ns, followed by a $2 \mu s$ long latching part at 90 % of the pulse height.
- **Drive and Measurement Lines:** The drive and readout microwave signals of each qubit are combined and sent to the sample through a pair of transmission lines that are attenuated by 70 dB over different temperature stages and filtered at 4 K and 300 mK. A microwave circulator at 20 mK separates the input signals going to the chip from the reflected signals coming from the chip. The latter are amplified by 36 dB at 4 K by two cryogenic HEMT amplifiers (CIT Cryo 1) with noise temperature 5 K. The reflected readout pulses get further amplified at room temperature and are then demodulated with the continuous signals of the readout microwave sources. The IQ quadratures of the demodulated signals are sampled at 1 GS/s by a 4-channel Data Acquisition system (Acqiris DC282).

II. TWO-QUBIT HAMILTONIAN

The Hamiltonian of a Cooper pair box j [s2, s1] with total Coulomb energy E_C^j (for a Cooper pair), with total Josephson energy $E_J^j(\phi_j)$, with island charge N_j (in Cooper pair units) and conjugated phase variable δ_j , biased by a gate charge $N_{g,j}$, is $H_j = E_C^j \left(\widehat{N}_j - N_{g,j} \right)^2 - E_J^j(\phi_j) \cos \left[\widehat{\delta}_j - \delta_{j,0}(\phi_j) \right]$ with $\tan(\delta_{j,0}) = d_j \tan(\pi \phi_j / \phi_0)$. In the limit $E_J^j \gg E_C^j$ [8] that corresponds to the transmon qubit and when restricting the Hilbert space to the two lowest eigenstates $\{|0\rangle_j, |1\rangle_j\}$, the $N_{g,j}$ parameters become irrelevant, and one has $\langle 0 | \widehat{N}_j | 0 \rangle \simeq \langle 1 | \widehat{N}_j | 1 \rangle \simeq 0$, $\langle 1 | \widehat{N}_j | 0 \rangle = 2^{-3/4} i \left(E_J^j / E_C^j \right)^{1/4}$, and $H_j = -h \nu_j \sigma_z^j / 2$ with $\nu_j \simeq \sqrt{2 E_C^j E_J^j(\phi_j)} / h$. When coupling two such transmon qubits by

a capacitance C_c much smaller than each total island capacitance, the total Hamiltonian is $H = H_1 + H_2 + H_{\text{int}}$ with $H_{\text{int}} = 2E_C^I E_C^{\text{II}} / E_{C_c} \hat{N}_1 \hat{N}_2$ and E_{C_c} the Coulomb energy of a Cooper pair on the coupling capacitor. Using the matrix elements above leads to $H_{\text{int}} = hg\sigma_y^I \sigma_y^{\text{II}}$ with $g = \sqrt{E_C^I E_C^{\text{II}} \nu_I \nu_{\text{II}} / (2E_{C_c})}$. This symmetric and purely transverse coupling term $\sigma_y^I \sigma_y^{\text{II}}$ (exchange term) is not surprising since each charge on a transmon island varying at the frequency of the other qubit plays the role of a resonant gate drive for this second qubit, and makes it rotate around an equatorial axis of its Bloch sphere. The precise YY nature (rather than XX for instance) is on the other hand meaningless and is a matter of initial convention for the global phases of the $|0\rangle$ and $|1\rangle$ states.

III. SAMPLE PARAMETERS

The sample is first characterized by spectroscopy (see Fig. 1.b of main text). The incident power used is high enough to observe the resonator frequency ν_R , the qubit line ν_{01} , and the two-photon transition at frequency $\nu_{02}/2$ between the ground and second excited states of each transmon (data not shown). A fit of the transmon model to the data yields the sample parameters $E_J^I/h = 36.2$ GHz, $E_C^I/h = 0.98$ GHz, $d_I = 0.2$, $E_J^{\text{II}}/h = 43.1$ GHz, $E_C^{\text{II}}/h = 0.87$ GHz, $d_{\text{II}} = 0.35$, $\nu_R^I = 6.84$ GHz, and $\nu_R^{\text{II}} = 6.70$ GHz. The qubit-readout anti crossing at $\nu = \nu_R$ yields the qubit-readout couplings $g_0^I \simeq g_0^{\text{II}} \simeq 50$ MHz. Independent measurements of the resonator dynamics (data not shown) yield quality factors $Q_I = Q_{\text{II}} = 730$ and Kerr non linearities [s3],[13] $K_I/\nu_R^I \simeq K_{\text{II}}/\nu_R^{\text{II}} \simeq -2.3 \pm 0.5 \times 10^{-5}$.

IV. READOUT CHARACTERIZATION

Errors in our readout scheme are discussed in detail in [13] for a single qubit. First, incorrect mapping $|0\rangle \rightarrow 1$ or $|1\rangle \rightarrow 0$ of the projected state of the qubit to the dynamical state of the resonator can occur, due to the stochastic nature of the switching between the two dynamical states. As shown in Fig. IV.1, the probability p to obtain the outcome 1 varies continuously from 0 to 1 over a certain range of drive power P_d applied to the readout. When the shift in power between the two $p_{|0\rangle,|1\rangle}(P_d)$ curves is not much larger than this range, the two curves overlap and errors are significant even at the optimal drive power where the difference in p is maximum. Second, even in the case of non overlapping $p_{|0\rangle,|1\rangle}(P_d)$ curves, the qubit initially projected in state $|1\rangle$ can relax down to $|0\rangle$ before the end of the measurement, yielding an outcome 0 instead of 1. The probability of these two types of errors vary in opposite directions as a function of the frequency detuning $\Delta = \nu_R - \nu > 0$ between the resonator and the qubit, so that a compromise has to be found for Δ . Besides, the contrast $c = \text{Max}(p_{|1\rangle} - p_{|0\rangle})$ can be increased [13] by shelving state $|1\rangle$ into state $|2\rangle$ with a microwave π pulse at frequency ν_{12} just before the readout resonator pulse. The smallest errors $e_0^{I,\text{II}}$ and $e_1^{I,\text{II}}$ when reading $|0\rangle$ and $|1\rangle$ are found for $\Delta_I = 440$ MHz and $\Delta_{\text{II}} = 575$ MHz and are shown by arrows in the top panels of Fig. IV.1: $e_0^I = 5\%$ and $e_1^I = 13\%$ (contrast $c_I = 1 - e_0^I - e_1^I = 82\%$), and $e_0^{\text{II}} = 5.5\%$ and $e_1^{\text{II}} = 12\%$ ($c_{\text{II}} = 82\%$). When using the $|1\rangle \rightarrow |2\rangle$ shelving before readout, $e_0^I = 2.5\%$ and $e_1^I = 9.5\%$ (contrast $c_I = 1 - e_0^I - e_1^I = 88\%$), and $e_0^{\text{II}} = 3\%$ and $e_1^{\text{II}} = 8\%$ ($c_{\text{II}} = 89\%$). These best results are very close to those obtained in [12], but are unfortunately not relevant to this work.

Indeed, when the two qubits are measured simultaneously, one has also to take into account a possible readout crosstalk, i.e. an influence of the projected state of each qubit on the outcome of the readout of the other qubit. We do observe such an effect and have to minimize it by increasing $\Delta_{I,\text{II}}$ up to ~ 1 GHz (where the dispersive shift $\chi \simeq 2.5$ MHz is still large enough), and by not using the shelving technique. An immediate consequence shown in Fig. IV.1(b) is a reduction of the $c_{I,\text{II}}$ contrasts. The errors when reading $|0\rangle$ and $|1\rangle$ are now $e_0^I = 19\%$ and $e_1^I = 7\%$ (contrast $c_I = 74\%$) and $e_0^{\text{II}} = 19\%$ and $e_1^{\text{II}} = 12\%$ (contrast $c_{\text{II}} = 69\%$). Then to characterize the errors due to crosstalk, we measure the 4×4 readout matrix \mathcal{R} linking the probabilities p_{uv} of the four possible uv outcomes to the population of the four $|uv\rangle$ states. As shown in Fig. IV.1(c-d), we then rewrite $\mathcal{R} = \mathcal{C}_{\text{CT}} \cdot (\mathcal{C}_I \otimes \mathcal{C}_{\text{II}})$ as the product of a 4×4 pure crosstalk matrix \mathcal{C}_{CT} with the tensorial product of the two 2×2 single qubit readout matrices

$$\mathcal{C}_{I,\text{II}} = \begin{pmatrix} 1 - e_0^{I,\text{II}} & e_1^{I,\text{II}} \\ e_0^{I,\text{II}} & 1 - e_1^{I,\text{II}} \end{pmatrix}.$$

In the worst case, the readout crosstalk is 2.1%. We also illustrate on the figure the impact of the readout errors on our swapping experiment by comparing the bare readout outcomes uv , the outcomes corrected from the independent readout errors only, and the $|uv\rangle$ population calculated with the full correction including crosstalk.

We now explain briefly the cause of the readout crosstalk in our processor. Unlike what was observed for other qubit readout schemes using switching detectors [5], the crosstalk we observe is not directly due to an electromagnetic perturbation induced by the switching of one detector that would help or prevent the switching of the other one.

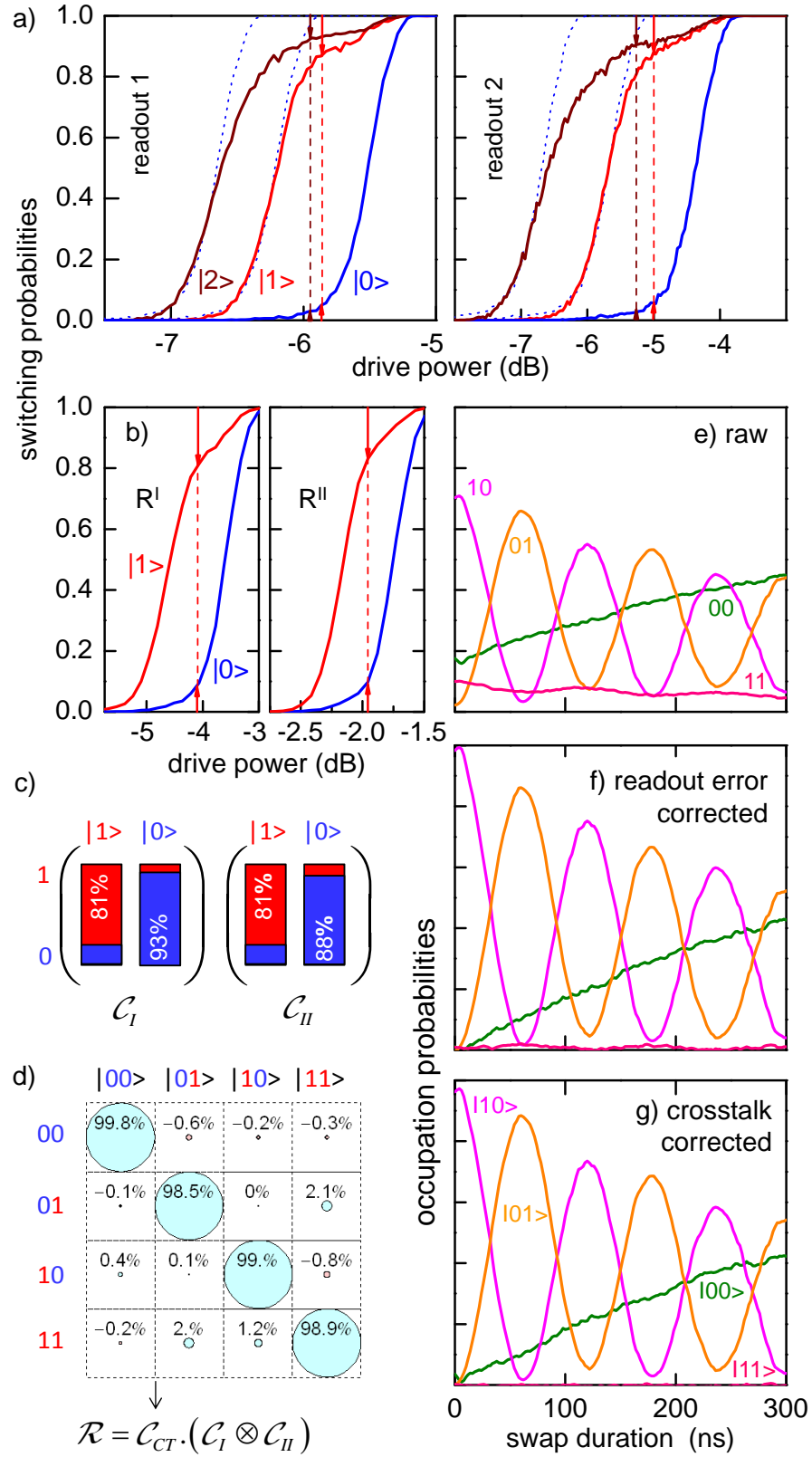


Figure IV.1: Readout imperfections and their correction. (a) Switching probabilities of the readouts as a function of their driving power, with the qubit prepared in state $|0\rangle$ (blue), $|1\rangle$ (red), or $|2\rangle$ (brown), at the optimal readout points. The arrows and dashed segments indicate the readout errors and contrast, at the power where the latter is maximum. (b) Same as (a) but at readout points $R^{I,II}$ used in this work. (c-d) Single readout matrices $\mathcal{C}_{I,II}$ and pure readout crosstalk matrix \mathcal{C}_{CT} characterizing the simultaneous readout of the two qubits. (e-g) bare readout outcomes uv , outcomes corrected from the independent readout errors only, and $|uv\rangle$ population calculated with the full correction including crosstalk for the swapping experiment of Fig. 2.

Indeed, when both qubits frequencies $\nu_{I,II}$ are moved far below $\nu_R^{I,II}$, the readout crosstalk disappears: the switching of a detector has no measurable effect on the switching of the other one. The crosstalk is actually due to the rather strong ac-Stark shift $\sim 2(n_H - n_L)g_0^2/(R - \nu_R) \sim 500$ MHz of the qubit frequency when a readout resonator switches from its low to high amplitude dynamical state with $n_L \sim 10$ and $n_H \sim 10^2$ photons, respectively. The small residual effective coupling between the qubits at readout can then slightly shift the frequency of the other resonator, yielding a change of its switching probability by a few percent. Note that coupling the two qubits by a resonator rather than by a fixed capacitor would solve this problem.

V. REMOVING ERRORS ON TOMOGRAPHIC PULSES BEFORE CALCULATING THE GATE PROCESS MAP

Tomographic errors are removed from the process map of our $\sqrt{i\text{SWAP}}$ gate using the following method. The measured Pauli sets corresponding to the sixteen input states are first fitted by a model including errors both in the preparation of the state (index *prep*) and in the tomographic pulses (index *tomo*). The errors included are angular errors $\varepsilon_{I,II}^{\text{prep}}$ on the nominal π rotations around $X_{I,II}$, $\eta_{I,II}^{\text{prep,tomo}}$ and $\delta_{I,II}^{\text{prep,tomo}}$ on the nominal $\pi/2$ rotations around $X_{I,II}$ and $Y_{I,II}$, a possible departure $\xi_{I,II}$ from orthogonality of (\vec{X}_I, \vec{Y}_I) and $(\vec{X}_{II}, \vec{Y}_{II})$, and a possible rotation $\mu_{I,II}$ of the tomographic XY frame with respect to the preparation one. The rotation operators used for preparing the states and for doing their tomography are thus given by

$$\begin{aligned} X_{I,II}^{\text{prep}}(\pi) &= e^{-i(\pi + \varepsilon_{I,II}^{\text{prep}})\sigma_x^{I,II}/2}, \\ X_{I,II}^{\text{prep}}(-\pi/2) &= e^{+i(\pi/2 + \eta_{I,II}^{\text{prep}})\sigma_x^{I,II}/2}, \\ Y_{I,II}^{\text{prep}}(\pi/2) &= e^{-i(\pi/2 + \delta_{I,II}^{\text{prep}})[\cos(\xi_{I,II})\sigma_y^{I,II} - \sin(\xi_{I,II})\sigma_x^{I,II}]/2}, \\ X_{I,II}^{\text{tomo}}(\pi/2) &= e^{-i(\pi/2 + \eta_{I,II}^{\text{tomo}})[\sin(\mu_{I,II})\sigma_x^{I,II} + \cos(\mu_{I,II})\sigma_y^{I,II}]/2}, \\ Y_{I,II}^{\text{tomo}}(-\pi/2) &= e^{+i(\pi/2 + \delta_{I,II}^{\text{tomo}})[\cos(\mu_{I,II} + \xi_{I,II})\sigma_y^{I,II} - \sin(\mu_{I,II} + \xi_{I,II})\sigma_x^{I,II}]/2}. \end{aligned}$$

The sixteen input states are then $\{\rho_{\text{in}}^e = U|0\rangle\langle 0|U^\dagger\}$ with $\{U\} = \{I_I, X_I^{\text{prep}}(\pi), Y_I^{\text{prep}}(\pi/2), X_I^{\text{prep}}(-\pi/2)\} \otimes \{I_{II}, X_{II}^{\text{prep}}(\pi), Y_{II}^{\text{prep}}(\pi/2), X_{II}^{\text{prep}}(-\pi/2)\}$, and each input state yields a Pauli set $\{\langle P_k^e \rangle = \text{Tr}(\rho_{\text{in}}^e P_k^e)\}$ with $\{P_k^e\} = \{I_I, X_I^e, Y_I^e, Z_I\} \otimes \{I_{II}, X_{II}^e, Y_{II}^e, Z_{II}\}$, $X^e = Y^{\text{tomo}}(-\pi/2)^\dagger \sigma_z Y^{\text{tomo}}(-\pi/2)$, and $Y^e = X^{\text{tomo}}(\pi/2)^\dagger \sigma_z X^{\text{tomo}}(\pi/2)$. Figure V.1 shows the best fit of the modeled $\{\langle P_k^e \rangle\}$ set to the measured input Pauli sets, yielding $\varepsilon_I^{\text{prep}} = -1^\circ$, $\varepsilon_{II}^{\text{prep}} = -3^\circ$, $\eta_I^{\text{prep}} = 3^\circ$, $\eta_{II}^{\text{prep}} = 4^\circ$, $\delta_I^{\text{prep}} = -6^\circ$, $\delta_{II}^{\text{prep}} = -3^\circ$, $\eta_I^{\text{tomo}} = -6^\circ$, $\eta_{II}^{\text{tomo}} = -4^\circ$, $\lambda_I^{\text{tomo}} = 12^\circ$, $\lambda_{II}^{\text{tomo}} = 5^\circ$, $\xi_I = 1^\circ$, $\xi_{II} = -2^\circ$, and $\mu_I = \mu_{II} = -11^\circ$.

Knowing the tomographic errors and thus $\{\langle P_k^e \rangle\}$, we then invert the linear relation $\{\langle P_k^e \rangle = \text{Tr}(\rho P_k^e)\}$ to find the 16×16 matrix B that links the vector $\overrightarrow{\langle P_k^e \rangle}$ to the columnized density matrix $\overrightarrow{\rho}$, i.e. $\overrightarrow{\rho} = B \cdot \overrightarrow{\langle P_k^e \rangle}$. The matrix B is finally applied to the measured sixteen input and sixteen output Pauli sets to find the sixteen $(\rho_{\text{in}}, \rho_{\text{out}})_k$ couples to be used for calculating the gate map.

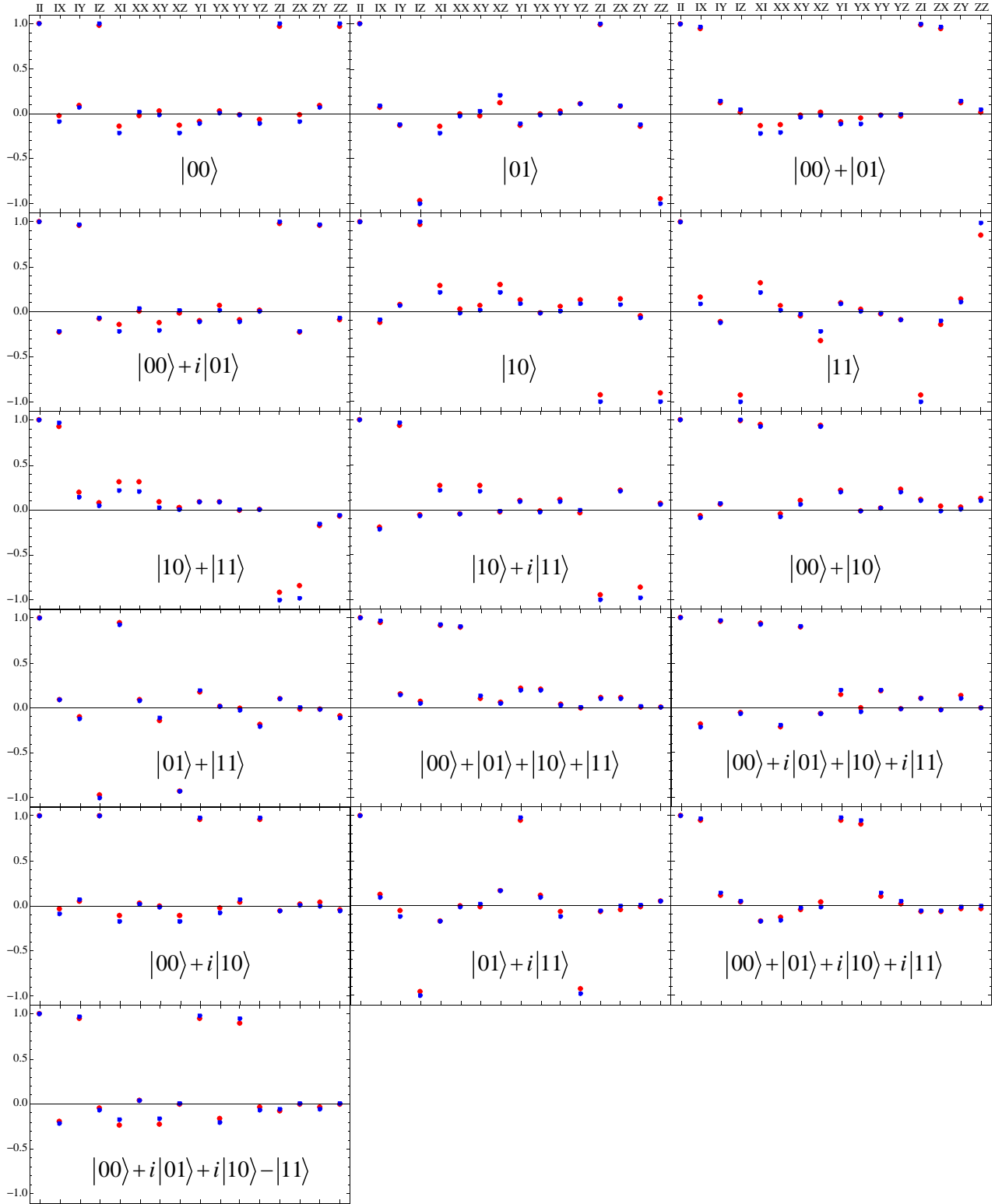


Figure V.1: Fitting of the pulse errors at state preparation and tomography. Measured (red) and fitted (blue - see text) Pauli sets $\langle P_k^e \rangle$ for the sixteen targeted input states $\{|0\rangle, |1\rangle, |0\rangle + |1\rangle, |0\rangle + i|1\rangle\}^{\otimes 2}$. The $\{II, IX, IY, IZ, XI, \dots\}$ operators indicated in abscissa are the targeted operators and not those actually measured (due to tomographic errors).

VI. REAL AND IMAGINARY PART REPRESENTATION OF THE MATRICES OF MAIN FIGURES 2 AND 4.

The ρ , χ and $\tilde{\chi}$ matrices of figures 2 and 4 of the main text are represented in an unconventional way that allows to encode both the modulus and the argument of each matrix element in the same matrix cell. Figures VI.1 to VI.3 show the same matrices using the more conventional real and imaginary part representation.

In addition, we show in Fig. VI.4 the contributions of relaxation, of inaccurate swapping time and of inaccurate rotations $\theta_{I,II}$ to the error matrix $\tilde{\chi}$. Contribution of relaxation is directly calculated from the independently measured values of the relaxation time T_1 , whereas the two other contributions result from a fit to the whole experimental $\tilde{\chi}$ matrix.

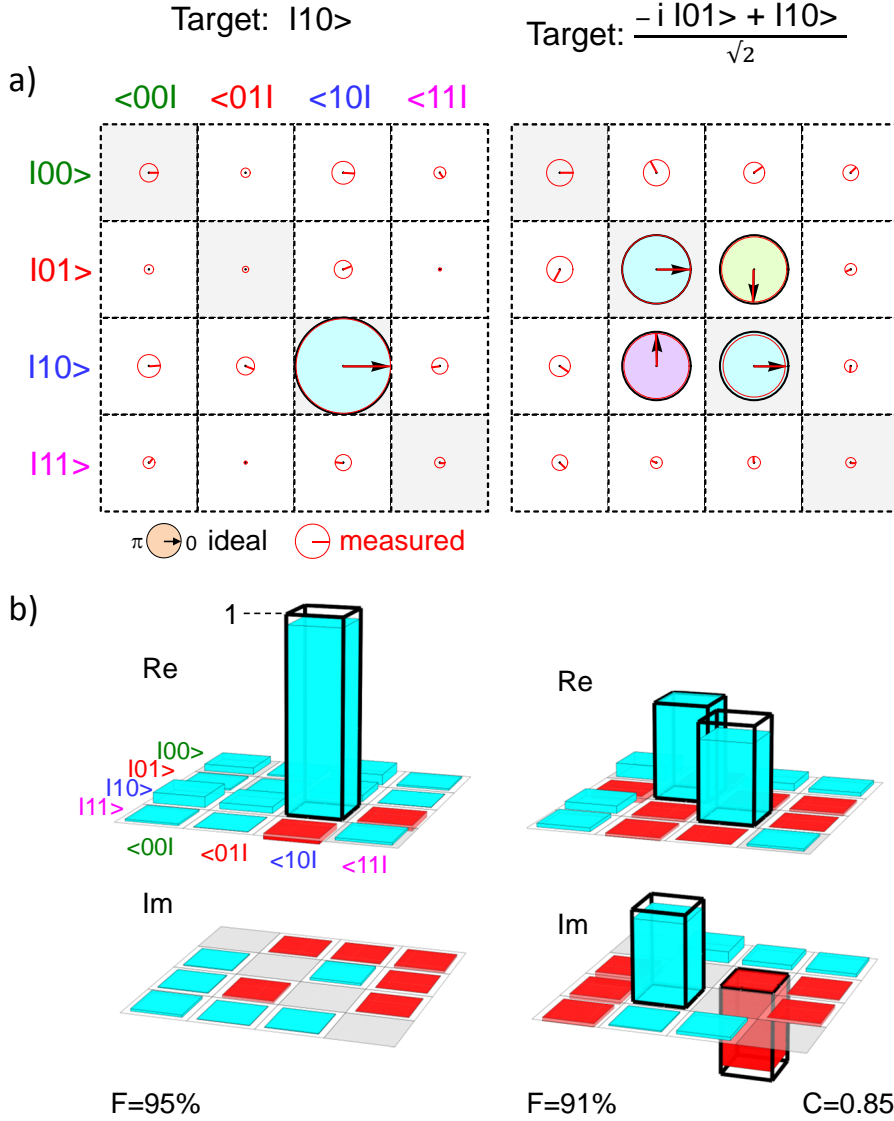
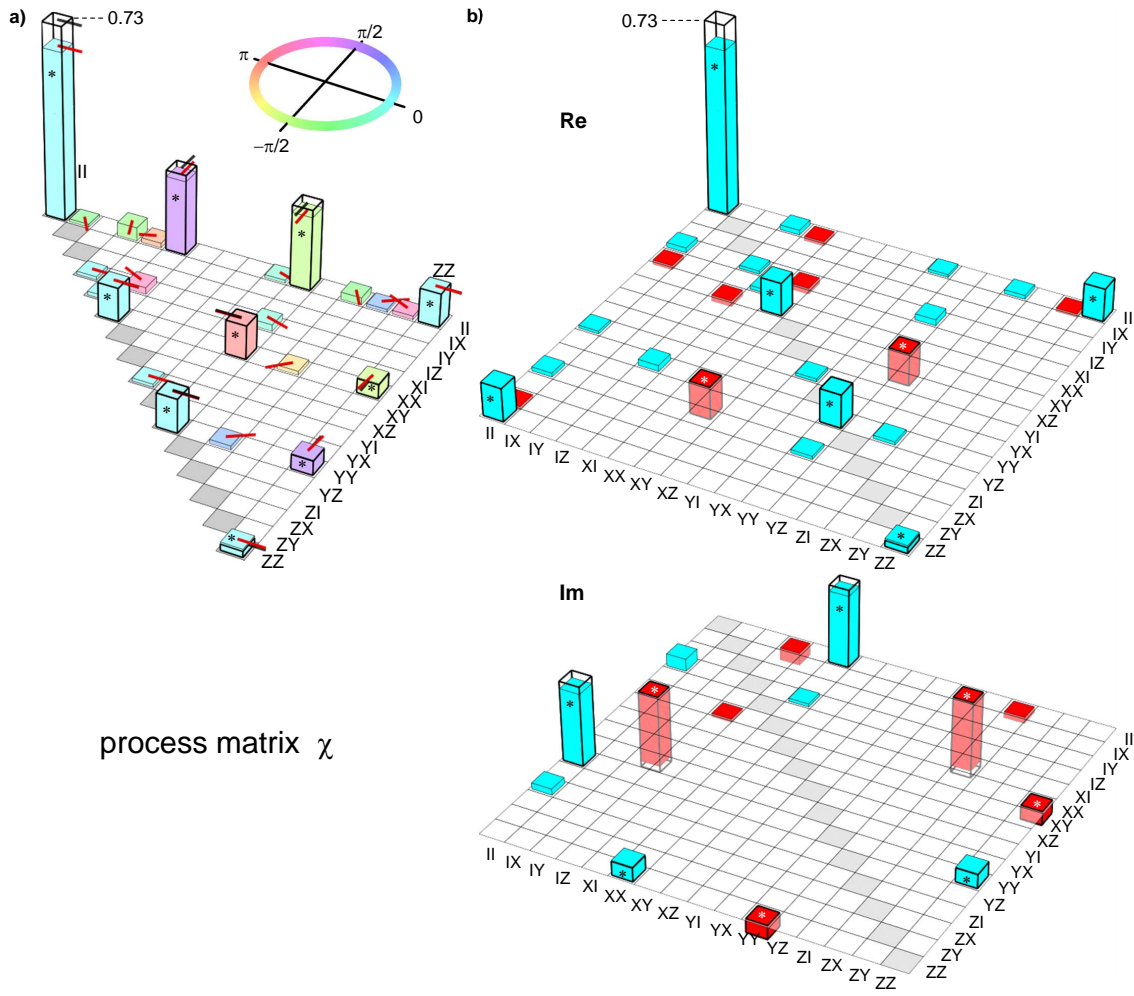


Figure VI.1: Same ideal and experimental density matrices as in Fig. 2, before and after one operation of the \sqrt{iSWAP} gate. (a) Color-filled black circles with black arrow is the ideal matrix whereas red circles and arrows is the experimental one. Each complex matrix element is represented by a circle with an area proportional to its modulus (diameter = cell size for unit modulus) and by an arrow giving its argument (usual trigonometric convention). (b) Real (top) and imaginary (bottom) parts of the same matrices, with positive and negative numbers being encoded along the vertical direction. The ideal matrix is represented by thick black empty bars, whereas experimental data are shown as blue-filled (positive) or red-filled (negative) thin bars.



process matrix χ

Figure VI.2: Same ideal and experimental process matrix χ as in Fig. 4(a). Expected elements are marked with a star and elements below 1% are not shown. (a) Each complex matrix element is represented by a bar with height proportional to its modulus and by an arrow at the top of the bar (as well as a filling color for the experiment - see top inset) giving its argument. (b) Real (top) and imaginary (bottom) parts of the same matrix, with positive and negative numbers being encoded along the vertical direction. The ideal matrix is represented by thick black empty bars, whereas experimental data are shown as blue-filled (positive) or red-filled (negative) thin bars.

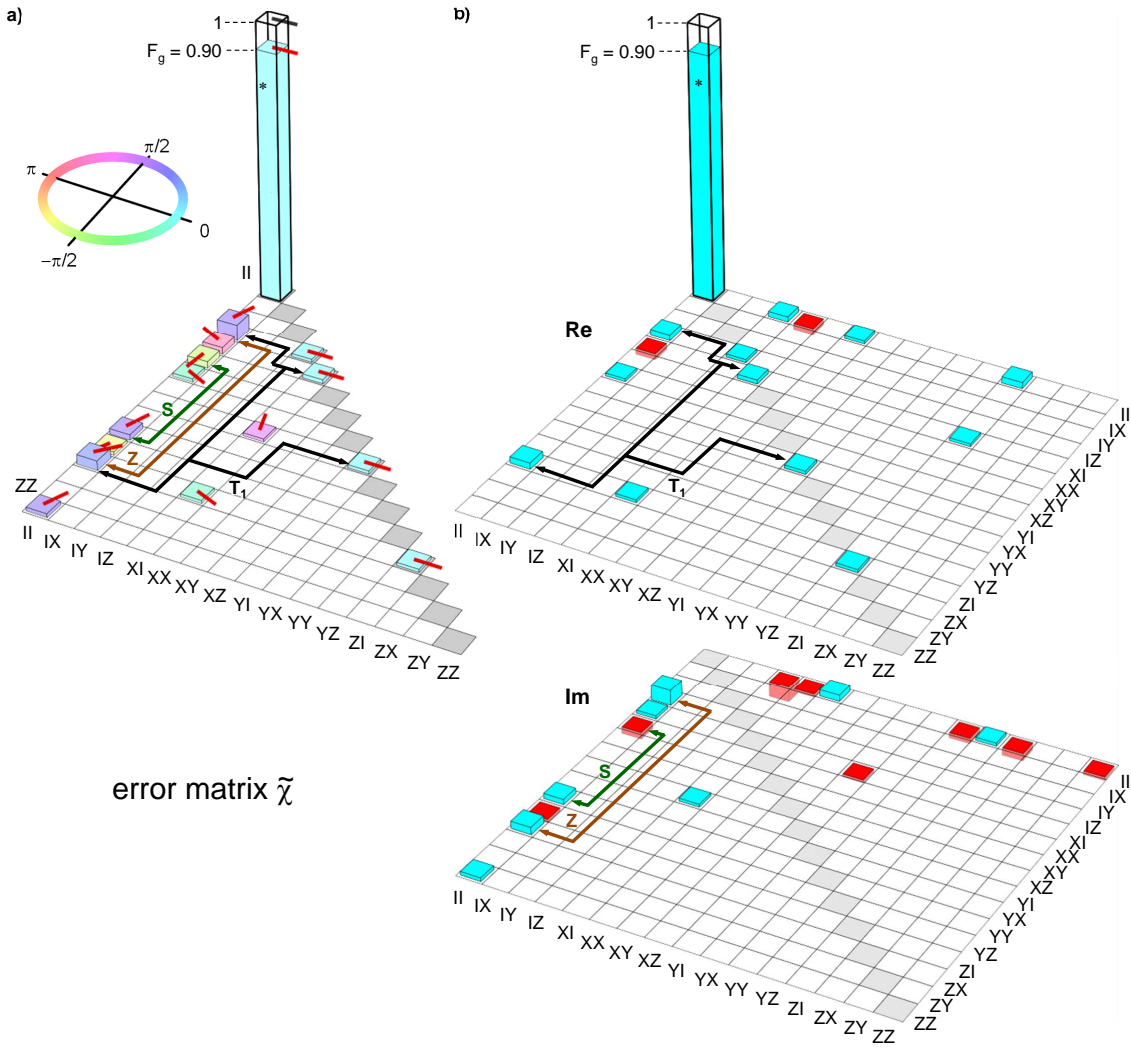


Figure VI.3: Same ideal and experimental error matrix $\tilde{\chi}$ as in Fig. 4(b). The $IIII$ matrix element is the only expected one; elements with modulus below 1% are not shown. (a) Each complex matrix element is represented by a bar with height proportional to its modulus and by an arrow at the top of the bar (as well as a filling color for the experiment - see left inset) giving its argument. (b) Real (top) and imaginary (bottom) parts of the same matrix, with positive and negative numbers being encoded along the vertical direction. The ideal matrix is represented by thick black empty bars, whereas experimental data are shown as blue-filled (positive) or red-filled (negative) thin bars. Labeled arrows indicate the main visible contributions to errors, i.e. a too long swapping time (S), too small rotations $\theta_{I,II}$ (Z), and relaxation (T_1).

[s1] D. Vion *et al.*, Science 296, 886 (2002).

[s2] A. Cottet, Ph.D. thesis, Universite Paris VI, 2002.

[s3] F. R. Ong *et al.*, Phys. Rev. Lett. 106, 167002 (2011).

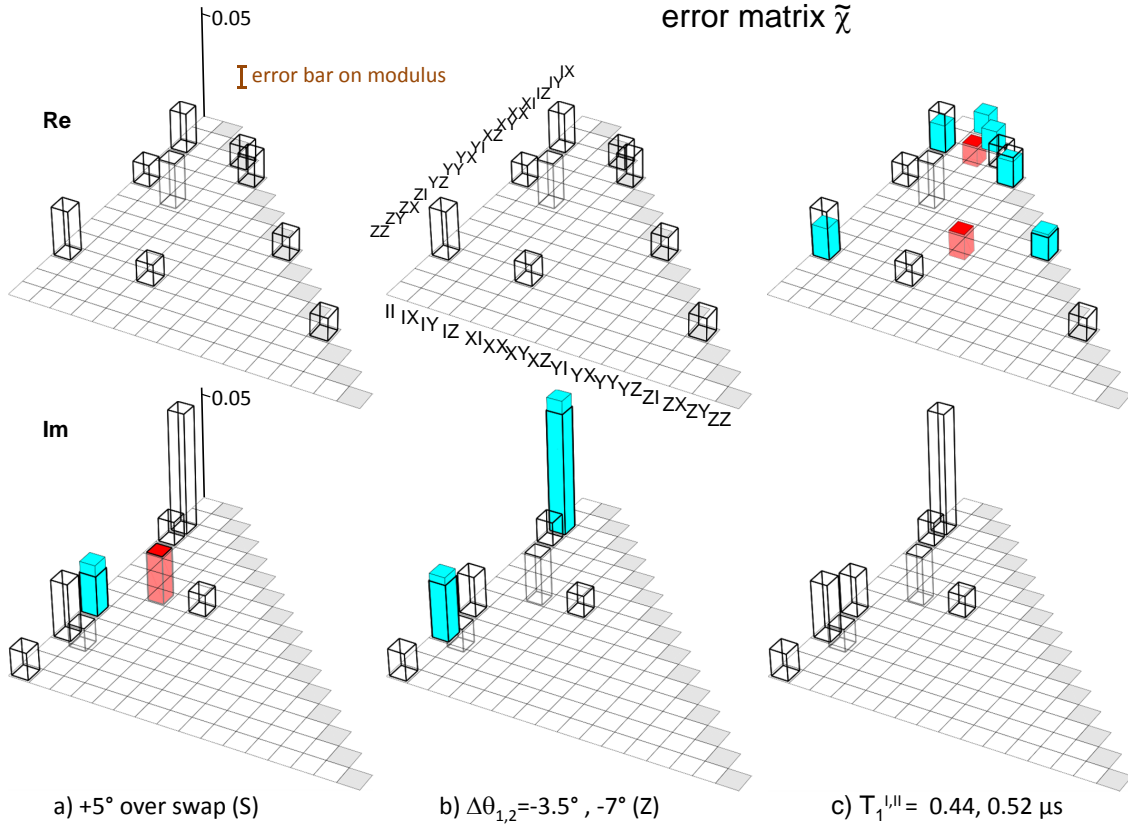


Figure VI.4: Experimental (empty bars) and calculated (color-filled thin bars) $\tilde{\chi}$ matrix for the three error contributions S, Z, and T_1 mentioned in the text and indicated in Figs. 4(b) and VI.3. Note that the vertical scale is expanded by a factor 10 with respect to other figures, and that matrix element $IIII$ as well as elements with modulus below the statistical error of 1% (see error bar) are not shown. Contribution T_1 is directly calculated from the independently measured values of the relaxation time T_1 , whereas contributions S and Z result from a fit to the whole experimental $\tilde{\chi}$ matrix (including the many small elements below 1%).